remote sensing

MDPI

Article

Carbon Dioxide Retrieval from TanSat Observations and Validation with TCCON Measurements

Shupeng Wang [1,2], Ronald J. van der A [2], Piet Stammes [2], Weihe Wang [1], Peng Zhang [1], Naimeng Lu [1], Xingying Zhang [1], Yanmeng Bi [1], Ping Wang [2] and Li Fang [3,*]

1 National Satellite Meteorological Center, China Meteorological Administration, Beijing 100081, China; wangsp@cma.cn (S.W.); wangwh@cma.cn (W.W.); zhangp@cma.cn (P.Z.); lunm@cma.cn (N.L.); zxy@cma.cn (X.Z.); biym@cma.cn (Y.B.)

2 Royal Netherlands Meteorological Institute (KNMI), 3731 GA De Bilt, The Netherlands; ronald.van.der.a@knmi.nl (R.J.v.d.A); piet.stammes@knmi.nl (P.S.); ping.wang@knmi.nl (P.W.)

3 Aerospace Information Research Institute, Chinese Academy of Sciences, Beijing 100101, China

* Correspondence: fangli@aircas.ac.cn

Received: 28 May 2020; Accepted: 7 July 2020; Published: 10 July 2020

Abstract: In this study we present the retrieval of the column-averaged dry air mole fraction of carbon dioxide (XCO_2) from the TanSat observations using the ACOS (Atmospheric CO_2 Observations from Space) algorithm. The XCO_2 product has been validated with collocated ground-based measurements from the Total Carbon Column Observing Network (TCCON) for 2 years of TanSat data from 2017 to 2018. Based on the correlation of the XCO_2 error over land with goodness of fit in three spectral bands at 0.76, 1.61 and 2.06 µm, we applied an a posteriori bias correction to TanSat retrievals. For overpass averaged results, XCO_2 retrievals show a standard deviation (SD) of ~2.45 ppm and a positive bias of ~0.27 ppm compared to collocated TCCON sites. The validation also shows a relatively higher positive bias and variance against TCCON over high-latitude regions. Three cases to evaluate TanSat target mode retrievals are investigated, including one field campaign at Dunhuang with measurements by a greenhouse gas analyzer deployed on an unmanned aerial vehicle and two cases with measurements by a ground-based Fourier-transform spectrometer in Beijing. The results show the retrievals of all footprints, except footprint-6, have relatively low bias (within ~2 ppm). In addition, the orbital XCO_2 distributions over Australia and Northeast China between TanSat and the second Orbiting Carbon Observatory (OCO-2) on 20 April 2017 are compared. It shows that the mean XCO_2 from TanSat is slightly lower than that of OCO-2 with an average difference of ~0.85 ppm. A reasonable agreement in XCO_2 distribution is found over Australia and Northeast China between TanSat and OCO-2.

Keywords: XCO_2; TanSat; ACOS; TCCON; full physical retrieval algorithm

1. Introduction

Atmospheric carbon dioxide (CO_2) along with methane (CH_4) and nitrous oxide (N_2O) are among the longest-lived greenhouse gases, with atmospheric lifetimes of decades [1]. CO_2 exhibits a larger radiative forcing on climate change than other greenhouse gases, which implies the great importance of monitoring global CO_2 sources and sinks. Global atmospheric CO_2 concentrations have increased by ~120 ppm over the last 200 years, largely due to human activities, such as fossil fuel combustion and land use changes [1]. Although surface CO_2 monitoring networks have expanded in recent decades, these observations remain insufficient for the limitations of low spatial coverage. These limitations have led to large uncertainties in climate predictions [2].

One of the most effective approaches to improve the spatial coverage and resolution for CO_2 monitoring is to use satellite measurements [3]. The thermal infrared observations of CO_2 from

satellite measurements including the Atmospheric Infrared Sounder (AIRS) [4], Infrared Atmospheric Sounding Interferometer (IASI) [5], and the Tropospheric Emission Spectrometer (TES) [6] can provide measurements of the atmospheric CO_2 column above 5 km. But these instruments have a limited sensitivity to CO_2 in the lower troposphere where the CO_2 sources and sinks resides [7]. The Scanning Imaging Absorption Spectrometer for Atmospheric Chartography (SCIAMACHY, which stopped working in April 2012) was able to measure the total CO_2 column on a global scale. It is also sensitive to CO_2 in the boundary layer [8]. However, these satellites were not exclusively designed for CO_2 monitoring. The Greenhouse Gases Observing SATellite (GOSAT) was the first CO_2 and CH_4 monitoring satellite launched on 23 January 2009 [9]. The other satellite designed for CO_2 observations, the Orbiting Carbon Observatory-2 (OCO-2), launched on 2 July 2014, can provide CO_2 measurements with a high spatial resolution of 3 km [10]. These two satellites are now yielding estimates of the column-averaged dry air mole fraction of carbon dioxide (XCO_2) with single sounding random errors between 0.1% and 0.3% (0.4 to 1.2 ppm) and systematic biases between 0.25% and 0.5% (1 to 2 ppm) over most of the globe [11,12]. High spatial resolution can not only provide more cloud-clear observations but also allow for monitoring of the CO_2 source in urban areas. China's first satellite to monitor atmospheric CO_2, TanSat, was launched on 22 December 2016. With three similar spectral bands and three similar observation modes of nadir, glint and target as OCO-2, TanSat can provide CO_2 measurements with 9 footprints along the swath at a fine spatial resolution of 2 km. The GOSAT-2 launched on 29 October 2018, is inherited from GOSAT and is able to perform measurements in five spectral bands, which can also achieve global CO observations. The latest Orbiting Carbon Observatory-3 (OCO-3) launched on 3 May 2019 is on board the International Space Station (ISS) and the observations of OCO-3 will be made for latitudes lower than 52 degrees. The measurements collected by OCO-2 and GOSAT are combined with CO_2 measurements from the ground-based network, such as the Total Column Carbon Observing Network (TCCON) [13], to obtain a better understanding of global CO_2 distribution and temporal variations.

The main problem in CO_2 retrievals is the specification of the light path, which is affected by aerosol scattering and surface reflection [14]. That is why the spectral measurements of Oxygen Absorption (O_2A) band are included in the CO_2 satellite missions. Near infrared and short-wave infrared measurements are both included for the simultaneous retrieval of the CO_2 concentration and of the scattering properties of aerosols or cloud particles. Buchwitz et al. [15] developed the Weighting Function Modified- Differential Optical Absorption Spectroscopy (WFM-DOAS) algorithm for CO_2 retrieval for SCIAMACHY. A low order polynomial is induced to simulate the slow variance signal, which is assumed to be mainly caused by ground reflectance and aerosol extinction. A rapidly varying signal, which is considered to be mainly caused by CO_2 absorption, is obtained by subtracting the slowly varying signal from the measured spectrum. Since the development of CO_2 observation sensors with much higher spectral resolutions, several research groups have developed full physics retrieval algorithms for CO_2 retrieval, including the National Institute for Environment Studies (NIES) [16–20], the Jet Propulsion Laboratory (JPL) of the National Aeronautics and Space Administration (NASA) [21,22], the University of Leicester (UoL) [23,24], the Netherlands Institute for Space Research (SRON) [25,26], the Institute of Atmospheric Physics in Chinese Academy of Science (IAP) [27], and the University of Bremen [28]. The algorithms developed by different institutes to retrieve CO_2 concentrations are based on similar inverse methods but using different settings for a priori information and using different aerosol models. The inverse method, which has been widely used in CO_2 retrievals, is based on an optimal estimation method that finds the most likely state vector from the best fit to the simulations and observations. The proper selection of the a priori constraints is critical for the retrieval accuracy.

The Atmospheric CO_2 Observations from Space (ACOS) algorithm was developed for CO_2 retrieval with OCO-2 data. And it has also been applied to GOSAT observations for CO_2 retrieval. The XCO_2 retrieval accuracy has been validated against TCCON measurements [12]. As the design of TanSat is similar to OCO-2, the ACOS algorithm is assumed to provide reliable XCO_2 retrievals

with TanSat measurements. In this paper, we apply the ACOS algorithm to TanSat measurements under nadir mode and evaluate the XCO_2 retrieval quality with the collocated ground-based TCCON measurements. For target mode, we collected TanSat observations of several cases and evaluate the XCO_2 retrieval results with a synchronous Unmanned Aerial Vehicle (UAV) experiment over Dunhuang calibration field (94.3208° E, 40.1375° N) and the measurements from ground-based Fourier-Transform Spectrometer (FTS) located in Beijing [29]. To exclude the low quality XCO_2 retrievals with large uncertainties (i.e., high aerosol loading, cloudy or large spectral uncertainties), we developed an a posteriori data filtering and an XCO_2 bias correction method for the bias between different footprints. A case where TanSat and OCO-2 have partly overlapping orbits is also investigated, where the XCO_2 regional distribution over Australia and northeast China between the different sensors are compared and discussed.

The paper is organized as follows: Section 2 describes the TanSat data and the validation datasets used in this work. The ACOS algorithm including the a posteriori data filtering and adjustments especially for TanSat measurements is described in Section 3. In Section 4, we validate the XCO_2 retrieval results under nadir mode using collocated TCCON measurements. The XCO_2 retrievals under target mode are also evaluated. Here, the performance of the bias correction is also discussed. Section 5 compares the XCO_2 spatial distribution over regions where TanSat and OCO-2 have overlapping orbits. Finally, Section 6 gives the conclusions.

2. Data Description

2.1. TanSat Observations

TanSat is a sun-synchronous polar-orbiting environmental satellite, with a local time of ~13:30, an orbit inclination of 98.16° and an orbit altitude of approximately 700 km. TanSat operates in three observational modes, including nadir, sun-glint, and target modes. TanSat carries two key instruments: The Atmospheric Carbon dioxide Grating Spectroradiometer (ACGS) and the Cloud and Aerosol Polarization Imager (CAPI). The ACGS was designed to measure solar radiation reflected in three different bands. The O_2A, ranging from 758 to 778 nm, includes the absorption of molecular oxygen, the weak absorption band of molecular carbon dioxide (WCO_2) ranges from 1594 to 1624 nm, and the strong absorption of carbon dioxide (SCO_2) band ranges from 2042 to 2082 nm. The spectral resolutions at the three bands defined as the Full Width at Half Maximum (FWHM) are ~0.04 nm, ~0.0131 nm and ~0.171 nm respectively. Within the FWHM, there are at least two samples in the direction of dispersion. The ACGS has a spatial resolution of 2 km × 3 km for nadir mode and nine footprints across the orbit, which makes a swath of ~20 km [29].

2.2. Validation Datasets

TanSat observations in nadir mode from January 2017 to December 2018 are collected. For nadir observations, all the exposures are used for XCO_2 retrieval. The a posteriori data filtering discussed in Section 4.1 is used to exclude the retrievals with large uncertainties. TCCON measurements are collocated with the TanSat nadir observations. The TCCON measures XCO_2 with an uncertainty lower than 0.25% [30]. The collocation criteria include a spatial distance of less than three degrees in both latitude and longitude direction and a time difference of less than two hours. For target mode observations, the view zenith angle should be smaller than 45 degrees.

The validation of retrievals with target mode is conducted using the ground-based FTS measurements in Beijing. The Beijing site is not part of the TCCON observation network. The site is operated by National Satellite Meteorological Center, China Meteorological Administration. The Bruker FTS 125HR in Beijing is similar to the equipment used at TCCON sites and has made observations since 2016 [31]. The precision of FTS CO_2 column has been reported to be better than 0.2% under clearsky conditions [31]; however, systemic bias needs be removed through continuous comparison withother FTS of TCCON sites. In April 2017, for validation of the TanSat target mode observation,

a synchronous UAV experiment was carried out over the Dunhuang calibration field. The CO_2 profile under ~5 km measured from Greenhouse Gas Analyzer (GGA) equipped on the UAV together with the CO_2 profile of higher layer obtained from the Carbon Tracker (CT) model [32] are integrated for XCO_2. The GGA CO_2 measurement uncertainty is smaller than 0.6 ppm and is ±0.08 ppm when averaging over 2000 s [33].

3. Retrieval Algorithm

The ACOS algorithm described in detail by O'Dell [21] has been developed for CO_2 retrievals with OCO data. Before the launch of OCO-2 it has been successfully applied to GOSAT data. After OCO-2 was launched in 2014, the algorithm has been used for the XCO_2 operational product and validated widely against ground-based measurements [12]. As the design of the ACGS is not exactly the same as of OCO-2, with a different band range, dynamic range and noise model, the algorithm had to be adjusted for the new instrument. When the measured radiances at all wavelengths in bands are included in the measurement vector y, it can be described as

$$\mathrm{y} = F(x, b) + \epsilon \tag{1}$$

where F is the forward transfer model, x is the state vector which contains all the parameters needed to be retrieved, and ϵ are the combined uncertainties from both instrument and forward model.

To find the state vector that produces the maximum a posteriori probability, we minimize the following standard cost function χ^2

$$\chi^2 = (y - F(x))^T {S_\epsilon}^{-1} (y - F(x)) + (x - x_a)^T {S_a}^{-1} (x - x_a) \tag{2}$$

S_ϵ is the measurement covariance matrix, S_a is the a priori covariance matrix, x_a is the a priori state vector.

For this nonlinear problem, we use an iterative way to find the solution as follows

$$\left((1+\gamma){S_a}^{-1} + {K_i}^T {S_\epsilon}^{-1} K_i\right) dx_{i+1} = \left[{K_i}^T {S_\epsilon}^{-1} (y - F(x_i)) + {S_a}^{-1} (x_a - x_i)\right] \tag{3}$$

$K = \frac{\partial F(x)}{\partial x}$ is the weighting function matrix, here we use the Levenberg-Marquardt modification of the Gauss-Newton method to find the best estimation of the state vector $\hat{x}$ iteratively [34]. γ is the Levenberg-Marquardt parameter, this method reduces to regular Gaussian-Newton minimization when $\gamma = 0$. γ is initialized with a value of 10.0 as used for OCO-2 [35].

As ACGS is sensitive to polarized light, the forward model should be able to simulate polarized light. The Lidort model [36] is used to simulate the multi-scattering radiance which is assumed to be unpolarized while the polarized light is simulated with the two Orders of Scattering (2OS) model [37]. Then the elements of the instrument Mueller matrix are used to put the stokes vector of the simulated polarized radiance at the Top Of Atmosphere (TOA) into the simulated radiance measured by the ACGS on the high resolution 0.01 cm^{-1} wavelength grid. The absorption coefficient spectroscopic database includes all the absorption lines of related gases used in the forward mode for the gas absorption cross-section calculation [35]. It includes the absorption lines in the O_2A band and CO_2 and H_2O absorption in the weak and strong CO_2 bands. In the forward model, the atmosphere is divided into 20 layers. Since the absorption cross-sections are nonlinear in both temperature and pressure within each layer, each atmospheric layer is subdivided into ten sub-layers; cross-sections for each are calculated for the interpolated pressure and temperature at the center of each sub-layer, converted to optical depth and then added to obtain the optical depth for each atmospheric layer.

For the modeling of atmospheric scattering, the algorithm retrieves a mixture of profiles of four fixed-type atmospheric scatters, which includes water cloud, ice cloud, dust aerosol, sea salt aerosol and stratospheric aerosol. To find the best combination of the five particles, the Aerosol Optical

Depths (AOD) at 755 nm of each component is retrieved in the algorithm. The forward model uses a Lambertian reflection over land and a wind-speed dependent COX-Munk reflectance for the ocean [38].

The retrieval algorithm requires a priori information on surface pressure, temperature profile, water vapor concentration and surface wind speed, which are interpolated from the European Centre for Medium Range Weather Forecasts (ECMWF) high-resolution 10-day forecast analysis data on a 0.125° × 0.125° grid. The interpolation is performed with linear interpolation in both time and space. 6-hourly global XCO_2 reanalysis products in 2016 and 2017 from Copernicus Atmosphere Monitoring Service (CAMS) are used as the XCO_2 a priori for the retrieval of 2017 and 2018, respectively. The a priori profiles for CO_2 are obtained by scaling the CO_2 profile derived from a multi-year global run of the Laboratoire de Météorologie Dynamique Zoom (LMDZ) model [39]. The monthly zonal mean is calculated from the model in 10° latitude bands. An offset is added to all the model values to make the global average surface value approximately equal to the measured value from GLOBALVIEW-CO_2 product (Co-operative Atmospheric Data Integration Project-Carbon Dioxide, 2005, ftp.cmdl.noaa.gov/ccg/co2/globalview/); this offset is updated monthly to reflect the increasing concentration of CO_2.

The solar irradiance data are obtained through a solar model which consists of two parts: the solar absorption model and the solar continuum model. The solar absorption model calculates the solar lines based on empirical solar line list which covers the 550–15,000 cm^{-1} spectrum and contains over 18,000 lines. The solar continuum model calculates the solar Planck function which is then multiplied with the solar absorption spectra to obtain the solar spectrum. The solar continuum model is based on a polynomial fit to the near-infrared part of the low resolution extra-terrestrial solar spectrum acquired by the SOLar SPECtrum (SOLSPEC) instrument [40].

The state vector is listed in Table 1.

Table 1. The State vector elements and their a priori values used in the retrieval.

State Vector Element	A Priori
AOD, aerosol layer height and spectral distribution width of five aerosol components	Merra database
Temperature profile offset	0
Surface pressure	ECMWF
Water vapor multiplier	1
Surface reflectance and the slope within the band of all three bands	estimated from TOA radiance
CO_2 profile	CAMS
Spectral dispersion offset at all three bands	0
Spectral dispersion slope at all three bands	1
Residual EOF amplitudes at all three bands	0

4. Validation

4.1. Retrieval Filters and Bias Correction

Table 2 gives the filters used in the TanSat retrieval to exclude retrieval results with large uncertainties, where Albedo_O_2A and Albedo_SCO_2 are the surface albedo in the O_2A band and SCO_2 band, respectively.

As we do not use the cloud mask product to screen out the exposure points contaminated by cloud, nearly 240 thousand exposure points of the TanSat nadir mode measurements are collocated with TCCON measurements and ~5.0% of these exposure points can obtain converged retrievals. After applying the filters listed in Table 2, 3320 effective retrievals (~1.5%) are found to be suitable retrievals used in the comparison with TCCON measurements.

Before the retrievals are used to compare with the TCCON measurements, we need to correct possible errors introduced by instruments, meteorology, a priori or retrieved parameters. The correction should be valid for each sounding. From our retrieval tests of the target mode, significant negative

biases are found for all nine footprints. The uncorrected XCO_2 retrievals show statistically differences ranging from −2.20 to −5.46 ppm with a Standard Deviation (SD) of 1.01 ppm. The errors arise from the calibration uncertainties in the Level 1 processing depending on the viewing direction in across-flight direction. As the 1st and 9th footprints have the smallest biases, we first correct the XCO_2 retrieval of the 1st and 9th footprints and then correct the retrievals of other footprints based on the corrected XCO_2 retrievals of these two footprints.

Table 2. Settings of the filters used for excluding low quality XCO_2 retrievals.

Parameters	Definition	Allowed Range
Sza	Solar zenith angle	<70 degrees
Vza	View zenith angle	<45 degrees
Iter	Maximum number of iterations	<8
DFS	Degrees of freedom for CO_2	>1.0
χ^2	Overall goodness of fit	<15.0
Blended albedo *	2.4 * Albedo_O_2A-1.13 * Albedo_SCO_2	<0.9
sev	Surface pressure variation	<400 pa
$\tau_{0.765}$	AOD at 765 nm	<0.8

* The blended albedo filter was first introduced in [41].

The retrieval bias of all footprints was found to be related with the reduced χ^2 in all 3 bands. The reduced χ^2 is defined as

$$\chi^2 = \frac{1}{(N - DFS)} \sum_{i=1}^{N} \left(\frac{y(i) - F(i)}{\sigma_i} \right) \tag{4}$$

where N is the number of wavelengths used in the retrieval, DFS is the degrees of freedom, $y(i)$ is the TanSat measurements, $F(i)$ is the simulated radiance and σ_i is the uncertainty of the TanSat measurement.

Through statistical analysis on two years of globally collocated retrievals with TCCON measurements in 2017 and 2018, it is found that $\frac{\chi^2_{O2}}{\chi^2_{sCO2}} > 1$ tends to lead to the high XCO_2 retrievals while $\frac{\chi^2_{O2}}{\chi^2_{sCO2}} < 1$ tends to lead to relatively low XCO_2 retrievals. Larger χ^2_{wCO2} will amplify the bias for the same $\frac{\chi^2_{O2}}{\chi^2_{sCO2}}$. We correct the bias of footprint-1 and -9 by

$$\begin{aligned} xco_2^{corr} &= xco_2 + c - k * \frac{\chi^2_{O2}}{\chi^2_{sCO2}} * \chi^2_{wCO2} \; \frac{\chi^2_{O2}}{\chi^2_{sCO2}} > 1.2 \\ xco_2^{corr} &= xco_2 + c \; 0.9 \le \frac{\chi^2_{O2}}{\chi^2_{sCO2}} \le 1.2 \\ xco_2^{corr} &= xco_2 + c + k * \frac{\chi^2_{O2}}{\chi^2_{sCO2}} * \chi^2_{wCO2} \; \frac{\chi^2_{O2}}{\chi^2_{sCO2}} < 0.9 \end{aligned} \tag{5}$$

where the coefficient k = 0.5 and c = 2.67. The coefficients are derived from the linear regression fit between retrievals and TCCON measurements. Then similar with the grid of CAMS, we divide the Earth into grid cells. The size of each grid cell is 4° × 4°. The whole TanSat orbit along the swath direction should be included within a certain grid cell. Then the XCO_2 retrievals with negative biases larger than 10 ppm from the a priori are excluded because they can be contaminated by cloud. But high XCO_2 retrievals are not excluded as it can be caused by an emission source. Then the averages of the XCO_2 retrievals for the 1st and 9th footprint are calculated as the mean XCO_2 of the grid. The correction of XCO_2 of the other footprints is conducted by correcting the mean XCO_2 of each footprint to the mean XCO_2 of the grid. The correction method works well to correct the bias between different footprints when the CO_2 variance in the grid is low. However, when the XCO_2 variance in the grid cell is high because there are both sources and sinks of CO_2 inside the same grid cell, the correction method may not be accurate enough.

Overall, after applying the bias correction method, the biases are largely reduced from −3.85 ppm to 0.27 ppm and the average sounding precisions σ is improved from 4.16 ppm to 2.25 ppm for retrievals

over land with the nadir mode. The bias corrections are intended to reduce mainly the instrument calibration biases.

4.2. TCCON Validation for TanSat Retrieval of Nadir Mode

In this section, the XCO_2 data retrieved with TanSat are validated against the collocated ground-based measurements at TCCON sites listed in Table 3. Figure 1 shows the comparison results over the two TCCON sites of Saga (130.28824° E, 33.24096° N) in Japan and Parkfalls (90.273° W, 45.945° N) in the United States of America (USA) with relatively more XCO_2 effective retrievals from TanSat in 2017 and 2018. Though there are some retrievals with relatively large uncertainties, most of the retrievals can represent the XCO_2 seasonal variance of the local areas around the TCCON sites. The bias is defined as the mean difference between the collocated TCCON and TanSat retrievals, the sounding retrieval precision (σ_t) defined as the SD of the difference and the station to station variability (σ_s) defined as the SD of the biases for different TCCON sites. Here only the land retrievals of the nadir view and target view modes are evaluated. It has been reported that the uncertainty of TCCON measurements is around 0.4 ppm for XCO_2 (1-sigma) [30]. For simplicity, in the following, the uncertainties of TCCON measurements are assumed to be consistent over all stations with the variability over the different sites to be zero [42,43].

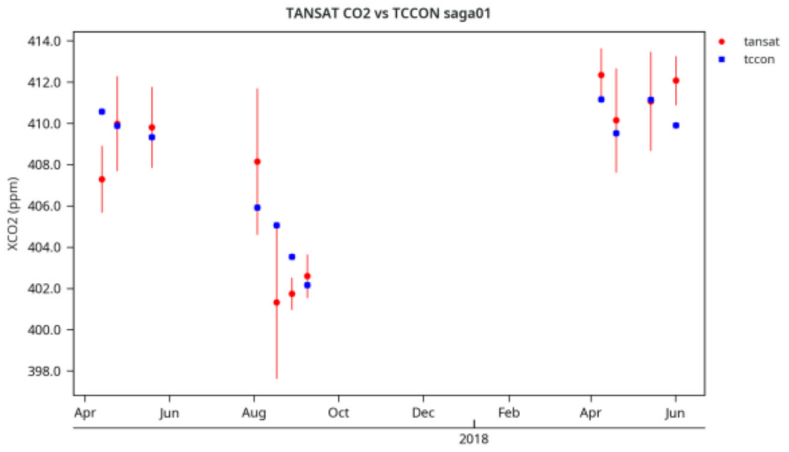

(**a**)

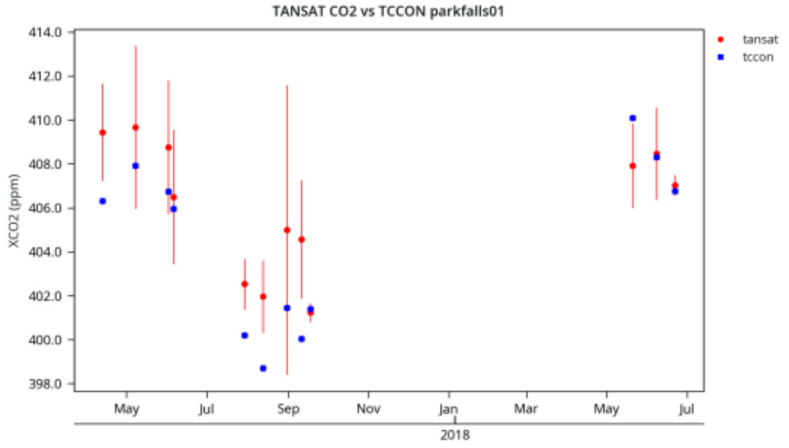

(**b**)

Figure 1. Time variation of XCO_2 retrieved from TanSat nadir observations over land (red dots) and collocated TCCON measurements (blue dots) for the stations of (**a**) Saga and (**b**) Parkfalls. SD of the TanSat retrievals are presented with the length of bar. All the retrievals shown here are bias-corrected.

Table 3. Geolocation and reference of each TCCON station used in comparison and validation.

Stations	Nationality	Latitude	Longitude	Reference
Sodankyla	Finland	67.3° N	26.6° E	[44]
Bialystok	Poland	53.2° N	23.0° E	[45]
Bremen	Germany	53.1° N	8.8° E	[46]
Karlsruhe	Germany	49.1° N	8.4° E	[47]
Park Falls	WI(USA)	48.4° N	2.3° E	[48]
Paris	France	48.4° N	2.3° E	[49]
Izana	Tenerife	48.4° N	2.3° E	[50]
Orleans	France	47.9° N	2.1° E	[51]
Garmisch	Germany	47.4° N	11.0° E	[52]
Rikubetsu	Japan	43.4° N	143.7° E	[53]
Lamont	OK(USA)	36.6° N	97.4° W	[54]
Tsukuba	Japan	36.0° N	140.1° E	[55]
Saga	Japan	33.2° N	130.2° E	[56]
Darwin	Australia	12.4° S	130.9° E	[57]
Wollongong	Australia	34.4° S	150.8° E	[58]
Burgos	Philippines	18.5° N	120.6° E	[59]
Edwards	USA	34.9° N	117.9° W	[60]
Jpl	USA	34.1° N	118.1° W	[61]
Pasadena	USA	34.1° N	118.1° W	[62]
Zugspitze	Germany	47.4° N	11.0° E	[63]

Figure 2 shows the comparison of the 3320 XCO_2 retrievals with TanSat against TCCON measurements. The average bias and SD are 0.41 ppm and 3.57 ppm respectively. It seems the retrievals tend to underestimate XCO_2 for the lower TCCON measurements around 405 ppm, while overestimate XCO_2 for higher XCO_2 measurements. That explains partly why the average bias is small. Figure 3 shows the overall comparison between the averaged TanSat retrievals and the TCCON measurements. For the averaged overpass results, the bias and SD are 0.27 ppm and 2.45 ppm respectively.

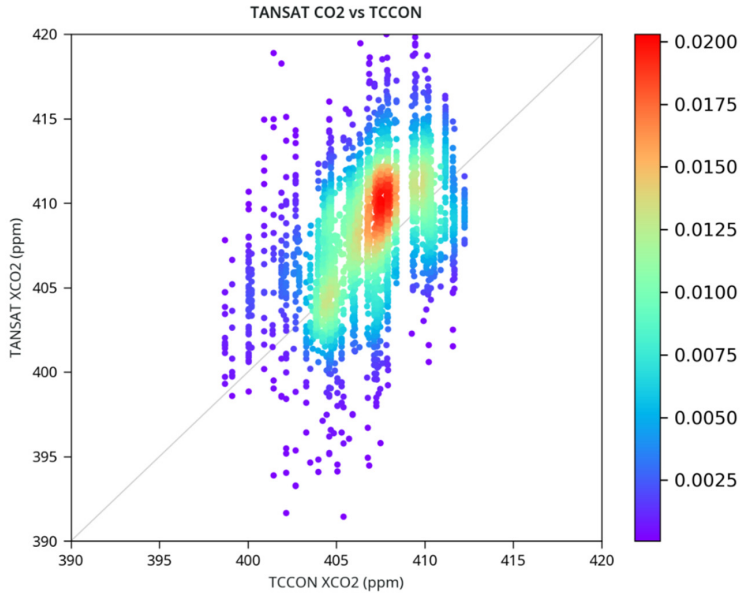

Figure 2. Validation of overall XCO_2 retrieved from TanSat nadir measurements over land with collocated TCCON data after bias correction. For retrievals collocated with multiple TCCON stations, we use data from the closest station. Different colors represent the normalized frequency of occurrence.

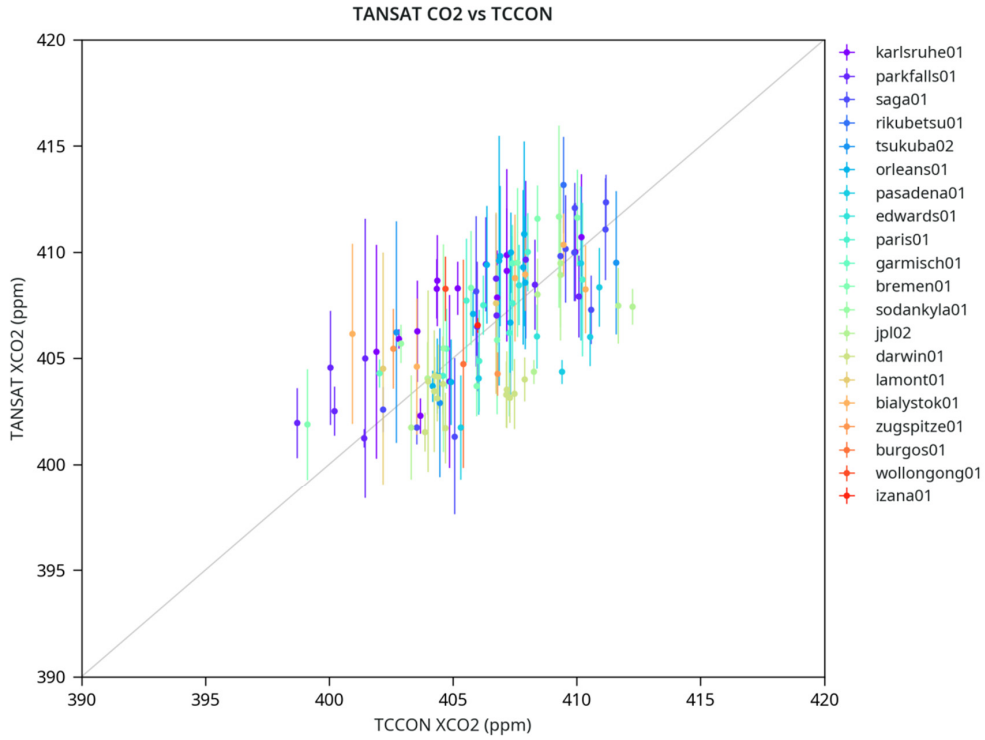

Figure 3. Validation of the averaged XCO_2 retrieved from TanSat nadir measurements with collocated TCCON data. The SD of the XCO_2 retrievals corresponding to each TCCON measurement scene is presented with the length of bar.

Figure 4 shows the biases of each TCCON stations as a function of latitude. The average bias and the average SD are 0.31 ppm and 2.50 ppm respectively, where stations with a number of collocations (N) less than two are not considered. It is found that the XCO_2 retrieval tends to be overestimated for regions north of 36° N and underestimated for regions south of 36° N. The averaged bias and SD of different sites north of 36° N are 1.30 ppm and 2.69 ppm respectively, while those of sites south of 36° N are −1.34 ppm and 2.22 ppm respectively. The SD for all the sites with N > 3 is smaller than 3 ppm. The SD of Darwin has the lowest SD of 1.74 ppm, while the SD of Orleans has the largest SD of 2.83 ppm. The SD of sites with latitudes north of 36° N are between 2.47 ppm at Karlsruhe and 2.87 ppm at Orleans. The SD of sites with latitude south of 36° N are between 1.74 ppm at Darwin and 2.04 ppm at Saga. For the retrievals south of 36° N, it is found that the average $\frac{\chi^2_{O2}}{\chi^2_{sCO2}}$ of 0.92 is lower than that of 1.73 for the retrievals north of 36° N. The average χ^2_{wCO2} are almost the same (1.92 and 1.87) for the retrievals south and north of 36° N respectively. As described in Section 4.1, the larger positive bias and relatively larger SD for the retrievals north of 36° N can be attributed to the larger $\frac{\chi^2_{O2}}{\chi^2_{sCO2}}$ that leads to overestimating XCO_2 and higher retrieval uncertainty. This trend may be related to the range of solar zenith angle and the different land cover types over the different latitudes. In the high latitude area, χ^2_{SCO2} is significantly smaller than that in the low latitude area (the averages are 2.26 and 3.46 respectively), and there is little difference in χ^2_{O2}. This phenomenon has also occurred in OCO-2, as [42] found there is a tendency for validations over stations in higher-latitude regions showing relatively larger biases in both the Northern and Southern hemispheres.

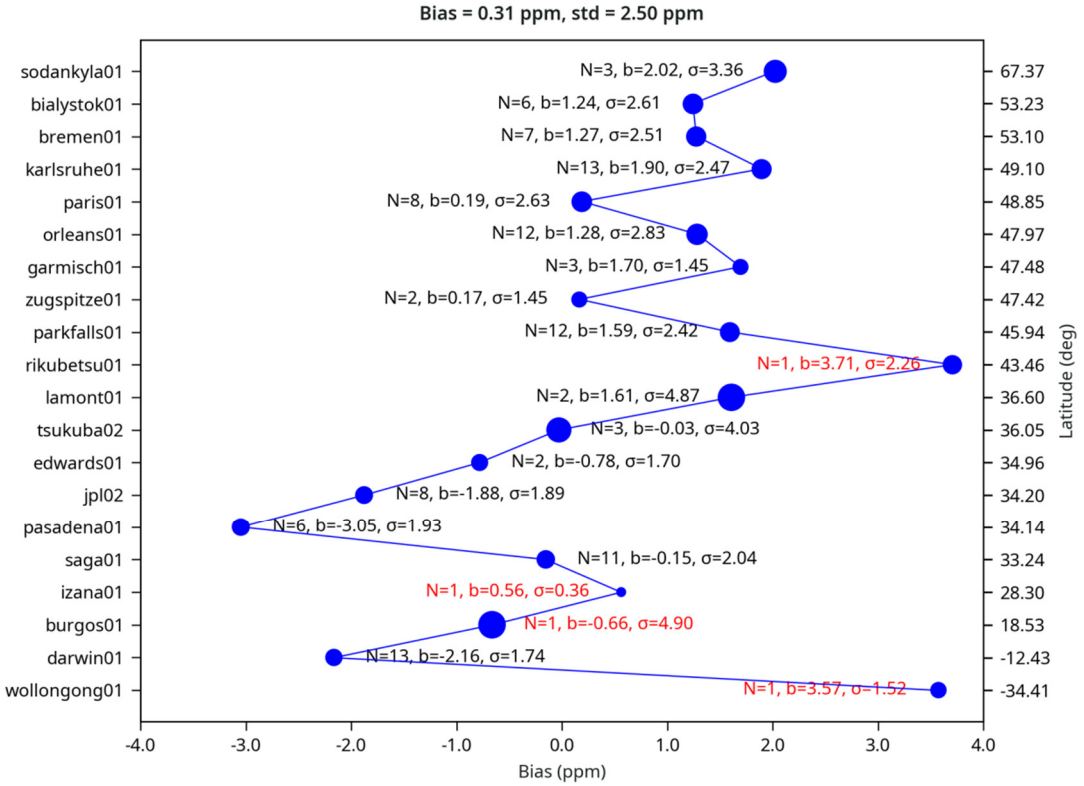

Figure 4. The bias of each TCCON site as a function of latitude. N is the number of collocations, b is the averaged bias, and σ is the averaged SD. The size of the blue dots indicates the value of σ. The std is the overall mean SD.

Figure 5 shows the time series of XCO_2 difference between TCCON measurements and averaged XCO_2 retrievals over the TCCON station with number of pixels/exposures > 3. The retrieval error here is obtained by subtracting the TCCON measurements from the XCO_2 retrieval results of TanSat. The average error of all stations in 2017 is 0.66 ppm, and that in 2018 is −0.27 ppm. Although there is no significant error change with different seasons and years at some stations such as Saga, the retrievals over many other stations, such as Darwin, Parkfalls, Karlsruhe and Orleans, show that the inversion error in 2018 has a negative offset compared with the inversion error in 2017. For Darwin, the mean error is −1.05 ppm in 2017 and −3.93 ppm in 2018. For Karlsruhe, the mean error is 2.95 ppm in 2017 and 0.20 ppm in 2018.

According to the XCO_2 bias correction method for TanSat described in Section 4.1, $\frac{\chi^2_{O2}}{\chi^2_{sCO2}}$ is the main parameter that affect the retrieval performance. The mean values of χ^2_{O2} in 2017 and 2018 are 3.9 and 2.9 respectively, while those of χ^2_{sCO2} are 2.7 and 2.5 respectively. Compared to the residuals in both bands in 2017, the residuals decreased in 2018. But the residual decrease in O2A band is larger than that in SCO2 band. It leads to the decrease of $\frac{\chi^2_{O2}}{\chi^2_{sCO2}}$ and the underestimation of XCO_2 in 2018. One possible reason is that the attenuation of O2A band is larger than that of SCO2 band. This phenomenon was also reported for OCO-2 retrievals [64], which show the fast signal degradation due to ice on the Focal Plane Arrays (FPA) leading to low sensitivity to TOA radiation. The fast signal degradation in the O_2A band is much stronger than in the two CO_2 bands. The correction of the attenuation needs further study.

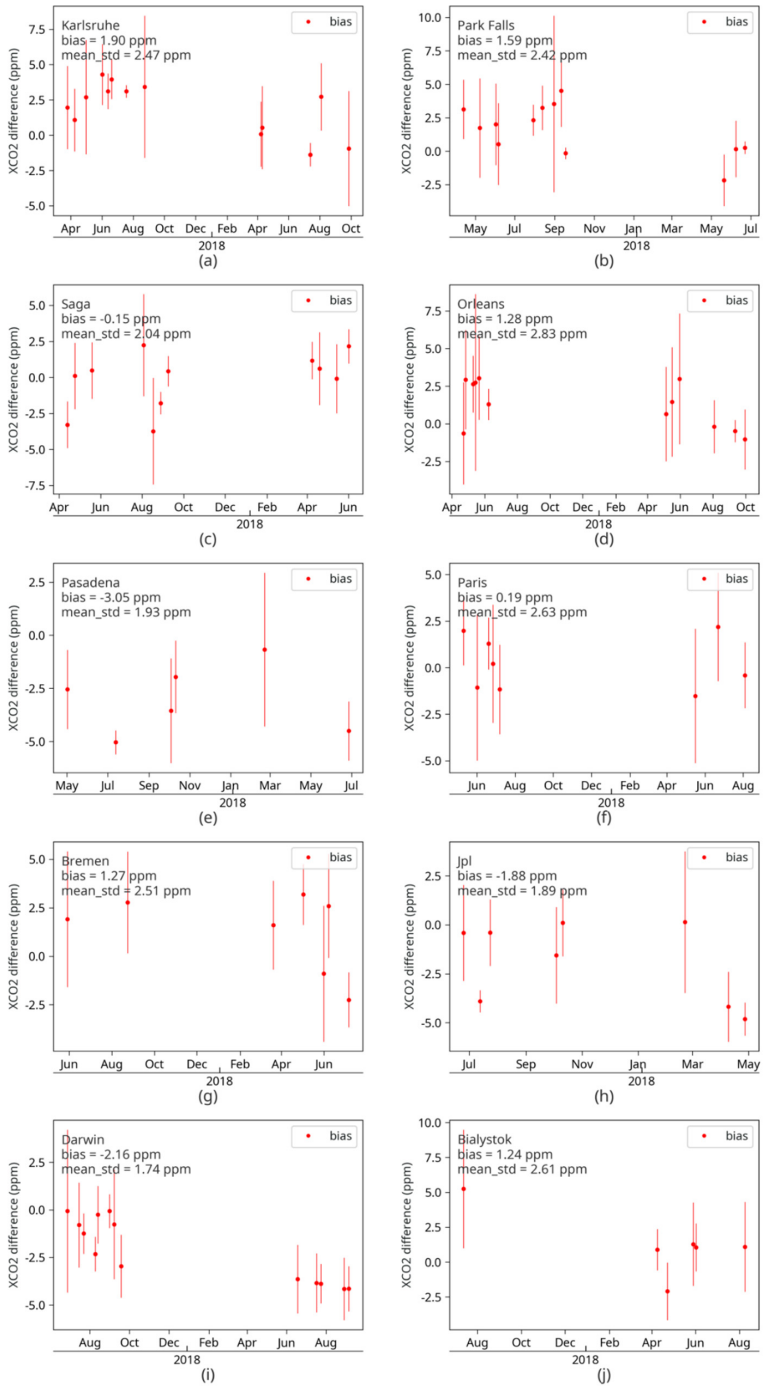

Figure 5. Time series of XCO_2 difference between retrievals from TanSat nadir observations over land and collocated TCCON measurements for each TCCON station: (**a**) Karlsruhe; (**b**) Park Falls; (**c**) Saga; (**d**) Orleans; (**e**) Pasadena; (**f**) Paris; (**g**) Bremen; (**h**) Jpl; (**i**) Darwin; (**j**) Bialystok. SD of individual TCCON measurement and satellite retrievals are presented with the length of bar. In each subplot, the overall bias, SD and site name are included. The results shown here are bias-corrected.

4.3. Case Study for TanSat Observation of Target Mode

The target mode observations of the TanSat were performed over the ground-based FTS in Beijing for one and a half year after its launch. A flight experiment was also carried out at Dunhuang calibration field in April 2017. As the TanSat instrument began to decay in 2018 (mentioned in Section 4.2), we present the TanSat validation results for target mode observations for three typical cases.

Case 1 gives the retrievals over Dunhuang calibration field. The Dunhuang calibration field is located in the Gobi Desert in northwest China, about 35 km west of Dunhuang City, Gansu Province. A synchronous flight experiment was conducted to collocate with the TanSat target observation over Dunhuang calibration field on 27 April 2017. A delta wing airplane with a powered parachute was used to measure the CO_2 profile. An UAV GGA [33] was installed on the plane for continuous CO_2, CH_4 and water vapor measurements. The flight duration was in the range of 1.7–2.3 h while spiral descent flights between 5 km and 0.1 km were carried out.

Despite the lack of FTS ground observations at the Dunhuang site, a ground-based GGA was installed at Dunhuang site during the experiment, together with a sun photometer to measure aerosol properties.

Figures 6 and 7 show the ground-based aerosol optical measurements and microphysical retrievals by Cimel Electronique-318 sun photometer at Dunhuang on 27 April 2017. AODs at 1.60 μm and 0.76 μm are 0.088 and 0.125, respectively. It can be concluded from the size distribution that the aerosol model is a fine-coarse mixture dominated by coarse particles.

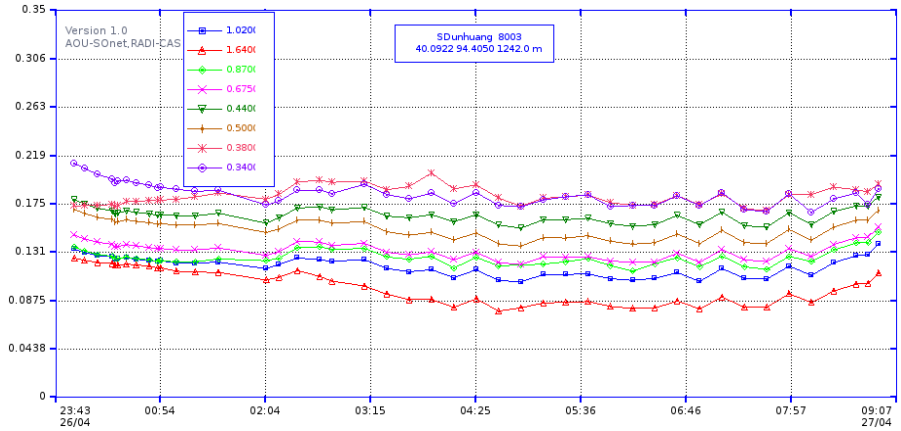

Figure 6. The ground-based measured spectral aerosol optical depths at Dunhuang on 27 April 2017 (UTC time).

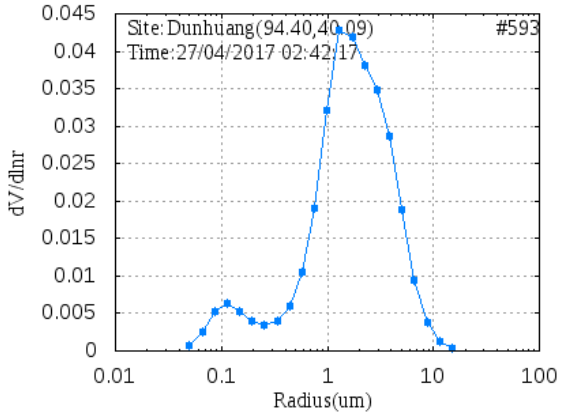

(**a**)

Figure 7. *Cont.*

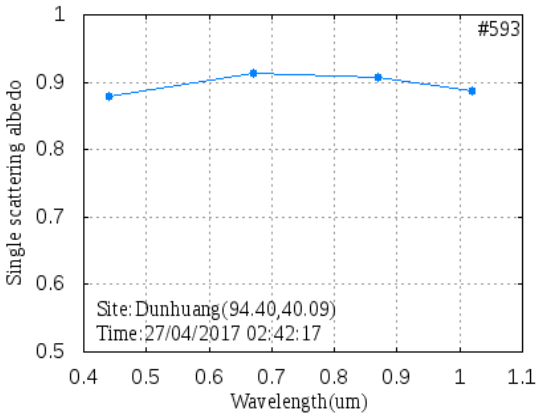

(**b**)

Figure 7. The aerosol properties retrieved at Dunhuang on 27 April 2017 including the (**a**) size distribution; and (**b**) single scattering albedo.

Figure 8 shows the CO_2 profiles observed by aircraft at 10:30 am and 3:00 pm (Beijing time, 8 h ahead of UTC time) near the overpass time of TanSat. The two CO_2 profiles are averaged to obtain the mean CO_2 profile at the overpass time of TanSat. In order to compare with the CO_2 column concentration retrieved by satellite, we interpolate the airplane measured CO_2 profiles to the layers used in the TanSat retrieval. The CO_2 profile above 5 km is obtained from the CT modelled profile. The CO_2 measurements on the ground are obtained from ground-based GGA. Then the XCO_2 for the aircraft in situ profile is calculated as follows:

$$X_{CO_2} = \sum_{i=1}^{N-1} h_i' \overline{u}_i \tag{6}$$

where N is the number of layer level boundaries, $N-1$ is the number of layers, h_i' is the weight function of each pressure layer. Finally, the integrated XCO_2 was 407.36 ppm and the uncertainty was estimated to be lower than 0.5 ppm.

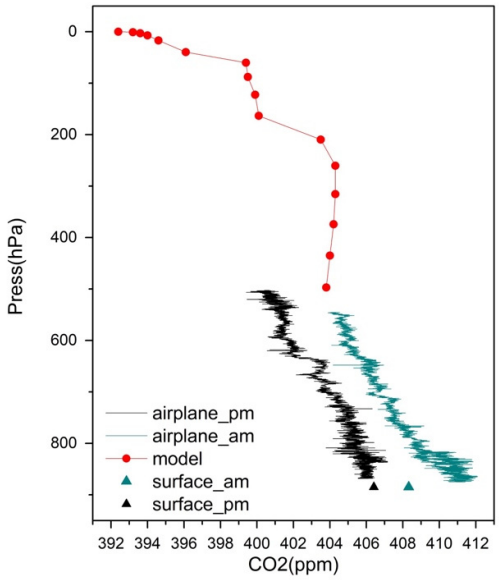

Figure 8. Combined CO_2 profile observed on 27 April 2017 over the Dunhuang calibration field. Black and green dots are the aircraft (in situ) data and the ground-based GGA data, respectively, obtained near the TanSat overpass time. The red line shows the CT modelled profile.

Figure 9 demonstrates the XCO_2 retrievals of the nine footprints of TanSat over Dunhuang. The mean and the SD of each footprint are also shown. We find that the average XCO_2 of footprint-5 to footprint-8 are overestimated and the bias range between 0.27 and 3.29 ppm. The average XCO_2 of the other footprints are underestimated and the biases range between −1.33 and −0.34 ppm. Except for the significantly high variance of footprint-6 (4.64 ppm), the variances of other footprints range between 0.67 and 1.27 ppm. The average XCO_2 of all footprints is 407.43 ppm and the bias was 0.06 ppm. With the exclusion of the footprint-6, the mean variance of the other footprints is 0.79 ppm.

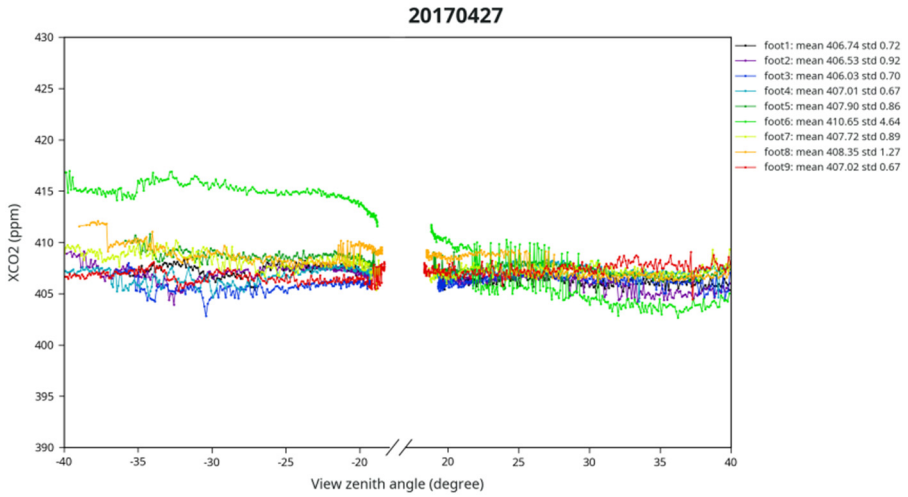

Figure 9. The retrieved XCO_2 of all 9 TanSat footprints over Dunhuang on 27 April 2017.

The following two cases show the XCO_2 retrievals over the ground-based FTS in Beijing (40.05° N, 116.28° E) on 4 and 31 May 2018, as shown in Figure 10. The AODs at 500 nm near the satellite overpass time on these two days are 0.63 and 0.20 respectively. The comparison of XCO_2 retrieval accuracy of these two days can indicate how the ACOS algorithm performs for the aerosol scattering correction. The XCO_2 observed by ground-based FTS is 415.50 ppm and 412.21 ppm on 4 and 31 May, respectively. The average XCO_2 of all footprints on 4 May is 413.26 ppm. The average bias and variance are −2.24 ppm and 1.65 ppm. The average XCO_2 of each footprint ranges between 413.36 ppm and 413.75 ppm. Except for the significantly higher variance of footprint-6 (3.3 ppm), the variances of other footprints range between 1.02 and 2.31 ppm. On 31 May, the average XCO_2 of all footprints is 412.06 ppm, and the average variance is 2.13 ppm. The bias from ground-based measurement is −0.15 ppm. The average XCO_2 of each footprint is between 411.79 ppm and 412.29 ppm. Except for the significantly higher variance of footprint-6 (3.58 ppm), the variance of other footprints range between 1.77 ppm and 2.54 ppm.

The comparison of the two cases in Beijing shows that ACOS algorithm performs well on correcting the uncertainty introduced by aerosol scattering. The average bias of the two-day retrieval results over Beijing is 2.09 ppm with similar variance. We also find that the footprint-6 has some significant system deviations compared with other footprints, probably due to the too many bad pixels for this footprint.

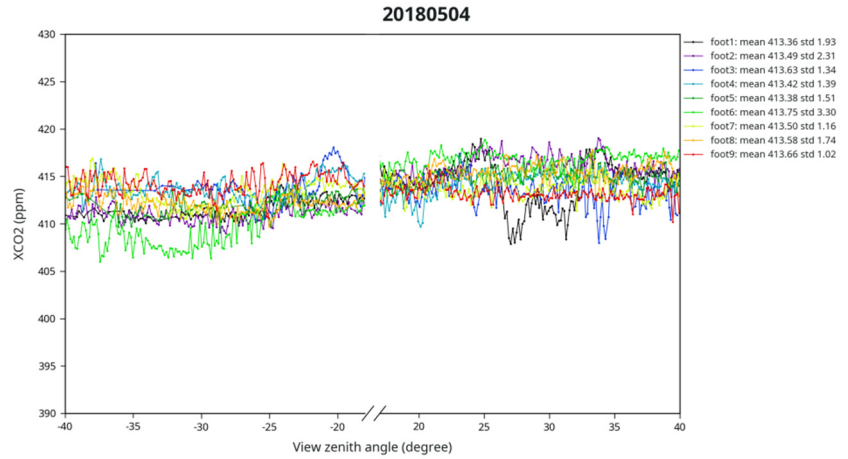

(**a**)

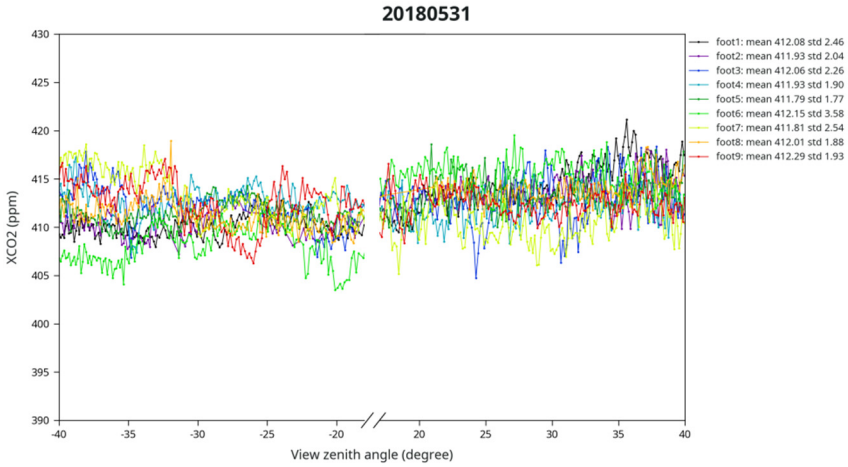

(**b**)

Figure 10. The retrieved XCO_2 of all 9 TanSat footprints over Beijing FTS on (**a**) 4 May and (**b**) 31 May 2018.

5. Comparison of the TanSat and OCO-2 Retrieval Results

In order to further evaluate the retrieval accuracy of TanSat nadir mode observations, the simultaneous XCO_2 retrieval products with TanSat and OCO-2 are compared. Figure 11 shows the orbital XCO_2 products of two satellites with overlapping regions on 20 April 2017. Figure 11a,b show the XCO_2 retrievals over Australia and Northeast China, respectively. In Australia, the average XCO_2 retrieved from TanSat and OCO-2 are 399.64 ppm and 400.48 ppm respectively, and the variances are 1.52 ppm and 1.17 ppm respectively. In the northeast of China, the mean XCO_2 retrieved from TanSat and OCO-2 are 408.52 ppm and 409.36 ppm respectively, and the variances are 3.15 ppm and 2.27 ppm respectively. In the two regions, the mean values of TanSat are slightly lower than OCO-2, with differences of 0.84 ppm and 0.86 ppm over Australia and Northeast China, respectively. And the variances of TanSat are slightly higher than OCO-2 with differences of 0.35 ppm and 0.88 ppm over Australia and Northeast China, respectively. It can be seen from the comparison that TanSat has relatively larger uncertainties than OCO-2, which may be attributed to signal-to-noise ratio of TanSat being lower than that of OCO-2 for the same retrieval bands. The deviation in retrieval bias between the two satellites is less than 1 ppm, therefore, it can be concluded that the XCO_2 products from two satellites agree well.

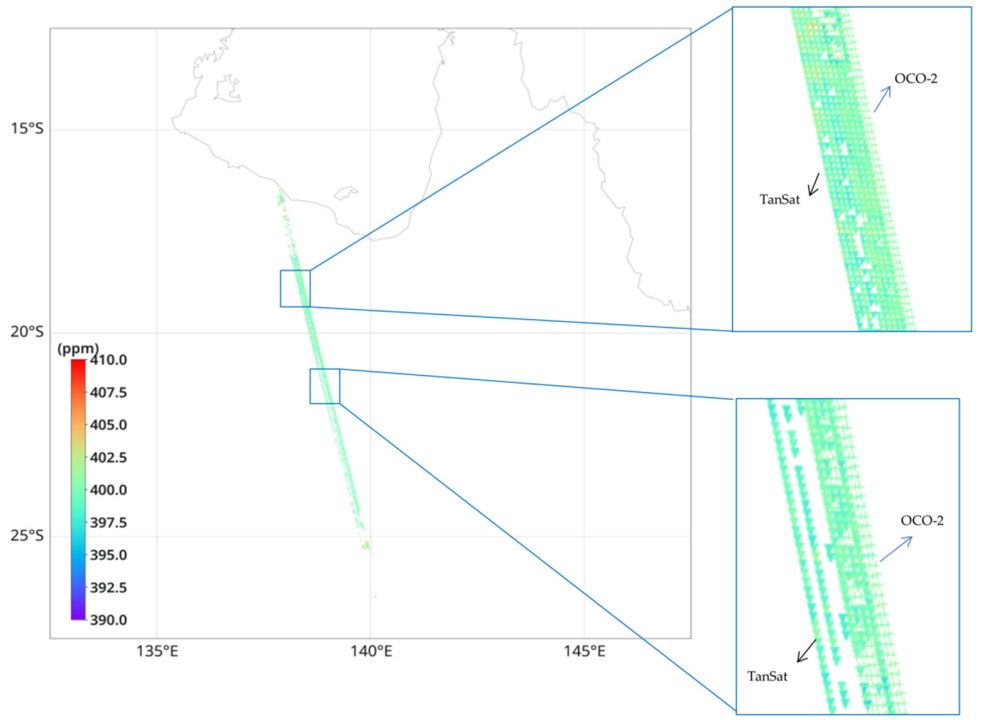

(**a**)

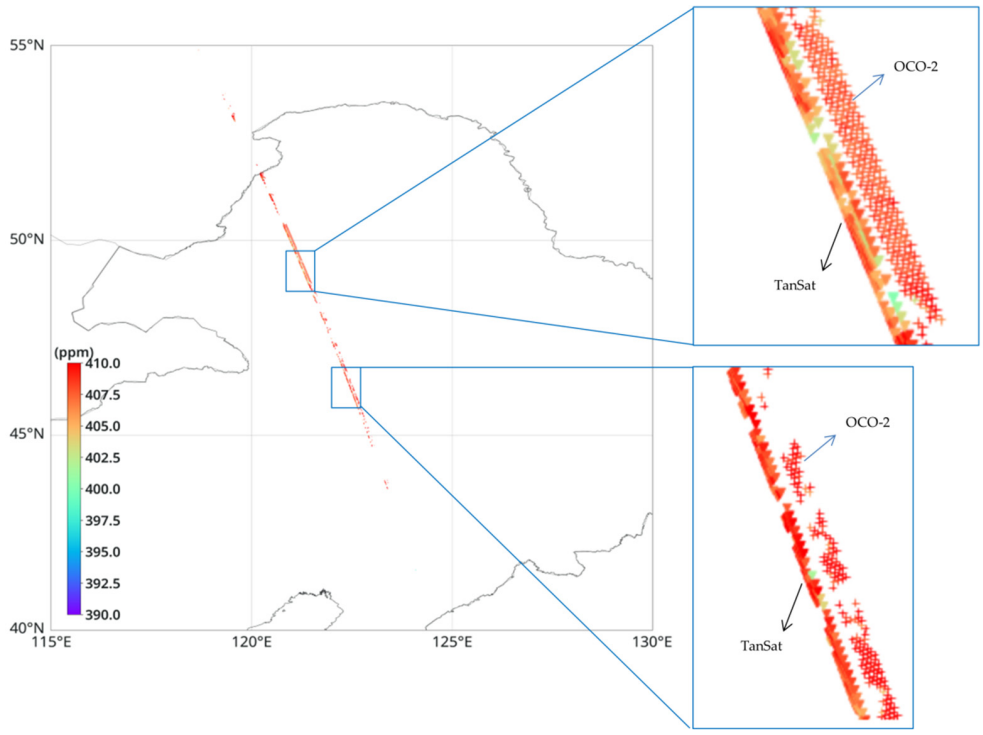

(**b**)

Figure 11. Comparison of the XCO_2 retrievals from TanSat and OCO-2 observations obtained using nadir mode on 20 April 2017. The XCO_2 retrievals from TanSat and OCO-2 are represented by triangle and cross respectively in (**a**) Australia and (**b**) Northeast China.

6. Conclusions

TanSat is China's first satellite specially used to detect CO_2 concentrations using near-infrared hyperspectral observations. The main on-board instrument ACGS can perform hyperspectral

measurements in O_2A band, CO_2 weak absorption band and CO_2 strong absorption band. Its design parameters are similar to those of OCO-2, and the observations can be obtained in nadir, target and glint modes. The ACOS, which is the CO_2 retrieval algorithm of OCO-2, has been successfully applied to OCO-2 and GOSAT. In this work, we apply the ACOS algorithm to TanSat measurements and evaluate the XCO_2 retrieval performance with various types of validation measurements.

The ACOS retrieval system is adjusted according to the instrument parameters and signal-to-noise ratio model of TanSat. Since we do not use the cloud detection product of TanSat to filter the cloud-contaminated observation before retrieval, we set strict post filter conditions to ensure the effectiveness of the retrieval. In nadir observation mode, we have collocated two years' TanSat observations and the ground-based TCCON measurements from 2017 to 2018. We obtained about 0.24 million matches, ~5% of all these observations reach converged retrievals. After applying the filter, 3320 effective retrievals (~1.5%) are considered as effective retrievals and used in the validation.

The average bias and SD are 0.41 ppm and 3.57 ppm respectively. If we average the retrievals of the same scene, 120 scenes are obtained. Then the average bias and SD decreased to 0.27 ppm and 2.45 ppm respectively. The bias of each TCCON station as a function of station latitude is also studied. It is found that the XCO_2 tends to be overestimated for regions north of 36° N in latitude while underestimated south of this latitude. The averaged bias and SD of various sites with latitude north of 36° N are 1.30 ppm and 2.69 ppm respectively, while those of sites south of 36° N are −1.34 ppm and 2.22 ppm respectively. The average bias of all stations is 0.66 ppm in 2017 and −0.27 ppm in 2018 respectively. The possible reason is that the attenuation in all three bands of TanSat intensified in 2018 and the attenuation in O_2A band is much stronger than that of the two CO_2 bands. It leads to relatively low sensitivity to the variance of CO_2 amount.

The analysis of the validation results of the target mode observations show that, the XCO_2 retrievals of the various TanSat footprints are underestimated. Based on the correlation between the retrieval error and the reduced χ^2 in all three bands, we propose a bias correction method. After applying the correction method, the bias is highly improved from −3.85 ppm to 0.27 ppm and the average variation is improved from 4.16 ppm to 2.25 ppm for land retrievals in nadir mode.

Three typical cases are investigated to validate the XCO_2 retrieval with TanSat target mode observations. In April 2017, the Dunhuang synchronous aircraft experiment showed that the retrieved XCO_2 is slightly overestimated with an average bias of all nine footprints being 0.06 ppm. Leaving out footprint-6, the mean variance of all footprints was 0.79 ppm. In 2018, two validation cases around the ground-based FTS in Beijing showed that the average biases are −2.24 and −0.15 ppm on 4 and 31 May respectively. On 4 May, the bias was obviously higher, probably because the AOD at 500 nm reached 0.63, which was much higher than the general retrieval condition (AOD < 0.3). The retrieval accuracy was influenced by the strong aerosol scattering. All the three cases show that the variance of footprint-6 is significantly larger than those of other footprints, and the detector of this footprint is apparently of lower quality.

In order to evaluate the regional distribution of the TanSat XCO_2, the simultaneous XCO_2 inversion products with TanSat and OCO-2 on 20 April 2017 are cross-compared. The comparison shows that the mean values of TanSat are slightly lower than OCO-2, with differences of 0.84 ppm and 0.86 ppm over Australia and Northeast China, respectively. And the variances of TanSat are slightly higher than OCO-2 with differences of 0.35 ppm and 0.88 ppm. It can be seen that TanSat retrievals show greater uncertainty than OCO-2, which may be due to a lower signal-to-noise of TanSat in the same band. The small deviation in XCO_2 products between the two satellites (less than 1ppm) show that the XCO_2 products from the two satellites agree well.

Author Contributions: Methodology, S.W.; software, S.W.; formal Analysis, S.W., R.J.v.d.A, P.S. and P.Z.; supervision, P.Z.; N.L. and W.W.; funding acquisition and project administration, W.W.; writing—original draft preparation, S.W.; validation, L.F.; writing—review & editing, R.J.v.d.A and L.F.; and visualization, L.F.; X.Z., Y.B. and P.W. provided the data for this study. All authors have read and agreed to the published version of the manuscript.

Funding: This research was supported by the National Key Research and Development Program of China (no. 2017YFC0209704), the National Natural Science Foundation of China (no. 41975032), and the National Key Research and Development Program of China (nos. 2017YFB0504001 and 2016YFA0600101).

Acknowledgments: We thank Minzheng Duan for providing the flight experiment data used in this study. We are also thankful to Zhongdong Yang for providing the Level 1B datasets of TanSat. The TCCON data were obtained from the TCCON Data Archive hosted by CaltechDATA at https://tccondata.org. We thank TCCON PIs for the TCCON measurements at stations of Bialystok, Bremen, Burgos, Darwin, Edwards, Garmisch, Izana, Jpl, Karlsruhe, Lamont, Orleans, Paris, Park Falls, Pasadena, Rikubetsu, Saga, Sodankyla, Tsukuba, Wollongong, and Zugspitze. The Paris TCCON site has received funding from Sorbonne Université, the French research center CNRS, the French space agency CNES, and Région Île-de-France. The TCCON stations at Rikubetsu, and Burgos are supported in part by the GOSAT series project. Local support for Burgos is provided by the Energy Development Corporation (EDC, Philippines). Darwin and Wollongong TCCON stations are supported by ARC grants DP160100598, LE0668470, DP140101552, DP110103118 and DP0879468. We thank OCO-2 team for the Level 2 XCO_2 products used in the comparison with XCO_2 retrievals from TanSat. We also thank the European Monitoring of Atmospheric Composition Change/CAMS projects for providing CO_2 model fields and the National Oceanic and Atmospheric Administration (NOAA) Earth System Research Laboratory (ESRL) for providing the CT data. We thank 4 anonymous reviewers for their advices on the improvement of the manuscript.

Conflicts of Interest: The authors declare no conflicts of interest.

References

1. Stocker, T.F.; Qin, D.; Plattner, G.K.; Tignor, M.; Allen, S.K.; Boschung, J.; Nauels, A.; Xia, Y.; Bex, V.; Midgley, P.M. *Climate Change 2013. The Physical Science Basis; Working Group I Contribution to the Fifth Assessment Report of the Intergovernmental Panel on Climate Change*; Cambridge University Press: Cambridge, UK, 2013.
2. Friedlingstein, P.; Meinshausen, M.; Arora, V.K.; Jones, C.D.; Anav, A.; Liddicoat, S.K.; Knutti, R. Uncertaintiesin CMIP5 climate projections due to carbon cycle feedbacks. *J. Clim.* **2014**, *27*, 511–526. [CrossRef]
3. Rayner, P.J.; O'Brien, D.M. The utility of remotely sensed CO_2 concentration data in surface source inversions. *Geophys. Res. Lett.* **2001**, *28*, 175–178. [CrossRef]
4. Crevoisier, C.; Heilliette, S.; Chédin, A.; Serrar, S.; Armante, R.; Scott, N.A. Midtropospheric CO_2 concentration retrieval from AIRS observations in the tropics. *Geophys. Res. Lett.* **2004**, *31*. [CrossRef]
5. Grieco, G.; Masiello, G.; Serio, C.; Jones, R.L.; Mead, M.I. Infrared atmospheric sounding interferometer correlation interferometry for the retrieval of atmospheric gases: The case of H_2O and CO_2. *Appl. Opt.* **2011**, *50*, 4516–4528. [CrossRef] [PubMed]
6. Engelen, R.J.; Andersson, E.; Chevallier, F.; Hollingsworth, A.; Matricardi, M.; McNally, A.P.; Thépaut, J.-N.; Watts, P.D. Estimating atmospheric CO_2 from advanced infrared satellite radiances within an operational 4D-Var data assimilation system: Methodology and first results. *J. Geophys. Res. Atmos.* **2004**, *109*. [CrossRef]
7. Bréon, F.M.; Ciais, P. Spaceborne remote sensing of greenhouse gas concentrations. *Comptes Rendus Geosci.* **2010**, *342*, 412–424. [CrossRef]
8. Buchwitz, M.; de Beek, R.; Noel, S.; Burrows, J.P.; Bovensmann, H.; Bremer, H.; Bergamaschi, P.; Korner, S.; Heimann, M. Carbon monoxide, methane, and carbon dioxide retrieved from SCIAMACHY by WFM-DOAS. *Atmos. Chem. Phys.* **2005**, *5*, 3313–3329. [CrossRef]
9. Yokota, T.; Yoshida, Y.; Eguchi, N.; Ota, Y.; Tanaka, T.; Watanabe, H.; Maksyutov, S. Global concentrations of CO_2 and CH_4 retrieved from GOSAT: First preliminary results. *SOLA* **2009**, *5*, 160–163. [CrossRef]
10. Crisp, D.; Atlas, R.; Breon, F.-M.; Brown, L.; Burrows, J.; Ciais, P.; Connor, B.; Doney, S.; Fung, I.; Jacob, D.; et al. The Orbiting Carbon Observatory (OCO) mission. *Adv. Space Res.* **2004**, *34*, 700–709. [CrossRef]
11. Buchwitz, M.; Dils, B.; Boesch, H.; Brunner, D.; Butz, A.; Crevoisier, C.; Detmers, R.; Frankenberg, C.; Hasekamp, O.; Hewson, W.; et al. ESA climate change initiative (CCI) product validation and intercomparison report (PVIR) for the essential climate variable (ECV) greenhouse gases (GHG) for data set climate research data package No. 4 (CRDP# 4). *Tech. Note* **2017**, *4*, 253. Available online: http://www.esa-ghg-cci.org/?q=node/95 (accessed on 28 May 2018).
12. Wunch, D.; Wennberg, P.O.; Osterman, G.; Fisher, B.; Naylor, B.; Roehl, C.M.; O'Dell, C.; Mandrake, L.; Viatte, C.; Kiel, M.; et al. Comparisons of the Orbiting Carbon Observatory-2 (OCO-2) XCO_2 measurements with TCCON. *Atmos. Meas. Tech.* **2017**, *10*, 2209–2238. [CrossRef]
13. Wunch, D.; Toon, G.C.; Blavier, J.-F.L.; Washenfelder, R.A.; Notholt, J.; Connor, B.J.; Griffith, D.W.; Sherlock, V.; Wennberg, P.O. The total carbon column observing network. *Philos. Trans. R. Soc. A* **2011**, *369*, 2087–2112. [CrossRef]

14. Aben, I.; Hasekamp, O.; Hartmann, W. Uncertainties in the space-based measurements of CO_2 columns due to scattering in the Earth's atmosphere. *J. Quant. Spectrosc. Radiat.* **2007**, *104*, 450–459. [CrossRef]
15. Buchwitz, M.; de Beek, R.; Noël, S.; Burrows, J.P.; Bovensmann, H.; Schneising, O.; Khlystova, I.; Bruns, M.; Bremer, H.; Bergamaschi, P.; et al. Atmospheric carbon gases retrieved from SCIAMACHY by WFM-DOAS: Version 0.5 CO and CH_4 and impact of calibration improvements on CO_2 retrieval. *Atmos. Chem. Phys.* **2006**, *6*, 2727–2751. [CrossRef]
16. Yoshida, Y.; Ota, Y.; Eguchi, N.; Kikuchi, N.; Nobuta, K.; Tran, H.; Morino, I.; Yokota, T. Retrieval algorithm for CO_2 and CH_4 column abundances from short-wavelength infrared spectral observations by the Greenhouse gases observing satellite. *Atmos. Meas. Tech.* **2011**, *4*, 717–734. [CrossRef]
17. Bril, A.; Oshchepkov, S.; Yokota, T.; Inoue, G. Parameterization of aerosol and cirrus cloud effects on reflected sunlight spectra measured from space: Application of the equivalence theorem. *Appl. Opt.* **2007**, *46*, 2460–2470. [CrossRef]
18. Oshchepkov, S.; Bril, A.; Yokota, T. PPDF-based method to account for atmospheric light scattering in observations of carbon dioxide from space. *J. Geophys. Res.* **2008**, *113*. [CrossRef]
19. Oshchepkov, S.; Bril, A.; Yokota, T. An improved photon path length probability density function–based radiative transfer model for space-based observation of greenhouse gases. *J. Geophys. Res.* **2009**, *114*. [CrossRef]
20. Oshchepkov, S.; Bril, A.; Maksyutov, S.; Yokota, T. Detection of optical path in spectroscopic space-based observations of greenhouse gases: Application to GOSAT data processing. *J. Geophys. Res.* **2011**, *116*. [CrossRef]
21. Crisp, D.; Fisher, B.; O'Dell, C.; Frankenberg, C.; Basilio, R.; Bosch, H.; Brown, L.R.; Castano, R.; Connor, B.; Deutscher, N.M.; et al. The ACOS CO_2 retrieval algorithm-Part II: Global XCO_2 data characterization. *Atmos. Meas. Tech.* **2012**, *5*, 687–707. [CrossRef]
22. O'Dell, C.W.; Connor, B.; Bösch, H.; O'Brien, D.; Frankenberg, C.; Castano, R.; Christi, M.; Eldering, D.; Fisher, B.; Gunson, M.; et al. The ACOS CO_2 retrieval algorithm–Part 1: Description and validation against synthetic observations. *Atmos. Meas. Tech.* **2012**, *4*, 99–121.
23. Boesch, H.; Baker, D.; Connor, B.; Crisp, D.; Miller, C. Global characterization of CO_2 column retrievals from shortwave-infrared satellite observations of the Orbiting Carbon Observatory-2 mission. *Remote Sens.* **2011**, *3*, 270–304. [CrossRef]
24. Connor, B.J.; Boesch, H.; Toon, G.; Sen, B.; Miller, C.; Crisp, D. Orbiting Carbon Observatory: Inverse method and prospective error analysis. *J. Geophys. Res.* **2008**, *113*. [CrossRef]
25. Butz, A.; Hasekamp, O.; Frankenberg, C.; Aben, I. Retrievals of atmospheric CO_2 from simulated space-bornemeasurements of backscattered near-infrared sunlight: Accounting for aerosol effects. *Appl. Opt.* **2009**, *48*, 3322–3336. [CrossRef] [PubMed]
26. Butz, A.; Guerlet, S.; Hasekamp, O.; Schepers, D.; Galli, A.; Aben, I.; Frankenberg, C.; Hartmann, J.M.; Tran, H.; Kuze, A.; et al. Toward accurate CO_2 and CH_4 observations from GOSAT. *Geophys. Res. Lett.* **2011**, *38*. [CrossRef]
27. Liu, Y.; Yang, D.X.; Cai, Z.N. A retrieval algorithm for TanSat XCO_2 observation: Retrieval experiments using GOSAT data. *Chin. Sci. Bull.* **2013**, *58*, 1520–1523. [CrossRef]
28. Heymann, J.; Reuter, M.; Hilker, M.; Buchwitz, M.; Schneising, O.; Bovensmann, H.; Burrows, J.; Kuze, A.; Suto, H.; Deutscher, N.M.; et al. Consistent satellite XCO_2 retrievals from SCIAMACHY and GOSAT using the BESD algorithm. *Atmos. Meas. Tech.* **2015**, *8*, 2961–2980. [CrossRef]
29. Yang, Z.; Zhen, Y.; Yin, Z.; Lin, C.; Bi, Y.; Liu, W.; Wang, Q.; Wang, L.; Gu, S.; Tian, L. Prelaunch Radiometric Calibration of the TanSat Atmospheric Carbon Dioxide Grating Spectrometer. *IEEE Trans. Geosci. Remote Sens.* **2018**, *56*, 4225–4233. [CrossRef]
30. Carbon Dioxide Information Analysis Center, Oak Ridge National Laboratory. *The Total Carbon Column Observing Network's GGG2014 Data Version*; Oak Ridge, TN, USA. 2015. Available online: https://data.caltech.edu/records/249 (accessed on 16 August 2019).
31. Yanmeng, B.; Qian, W.; Zhongdong, Y.; Jie, C.; Wenguang, B. Validation of column-averaged dry air mole fraction of CO_2 retrieved from OCO-2 using ground-based FTS measurements. *J. Meteor. Res.* **2018**, *32*, 433–443. [CrossRef]
32. Peters, W.; Jacobson, A.R.; Sweeney, C.; Andrews, A.E.; Conway, T.J.; Masarie, K.; Miller, J.B.; Bruhwiler, L.M.; Pétron, G.; Hirsch, A.I.; et al. An atmospheric perspective on North American carbon dioxide exchange: Carbon Tracker. *Proc. Natl. Acad. Sci. USA* **2007**, *104*, 925–930. [CrossRef]

33. Berman, E.S.F.; Fladeland, M.; Liem, J.; Kolyer, R.; Gupta, M. Greenhouse gas analyzer for measurements of carbon dioxide, methane, and water vapor aboard an unmanned aerial vehicle. *Sens. Actuators B Chem.* **2012**, *169*, 128–135. [CrossRef]
34. Fletcher, R. *A Modified Marquardt Subroutine for Nonlinear Leastsquares Fitting*; Atomic Energy Research Establishment: Harwell, UK, 1971.
35. Crisp, D.; Bosch, H.; Brown, L.; Castano, R.; Christi, M.; Connor, B.; Frankenberg, C.; McDuffie, J.; Miller, C.E.; Natraj, V.; et al. *OCO (Orbiting Carbon Observatory)-2 Level 2 Full Physics Retrieval Algorithm Theoretical Basis*; Tech. Rep. OCO D-65488; NASA Jet Propulsion Laboratory, California Institute of Technology: Pasadena, CA, USA, 2010; version 1.0 Rev 4. Available online: http://disc.sci.gsfc.nasa.gov/acdisc/documentation/OCO-2_L2_FP_ATBD_v1_rev4_Nov10.pdf (accessed on 25 November 2017).
36. Spurr, R.J.D.; Kurosu, T.P.; Chance, K.V. A linearized discrete ordinate radiative transfer model for atmospheric remote-sensing retrieval. *J. Quant. Spectrosc. Radiat.* **2001**, *68*, 689–735. [CrossRef]
37. Natraj, V.; Spurr, R.J.D. A fast linearized pseudo-spherical two orders of scattering model to account for polarization in vertically inhomogeneous scattering absorbing media. *J. Quant. Spectrosc. Radiat.* **2007**, *107*, 263–293. [CrossRef]
38. Cox, C.; Munk, W. Statistics of the sea surface derived from sun glitter. *J. Mar. Res.* **1954**, *13*, 198–227.
39. Hourdin, G.; Talagrand, O. Eulerian backtracking of atmospheric tracers. I: Adjoint derivation and parameterization of sub-grid scale transport. *Meteorol. Soc.* **2006**, *132*, 567–583. [CrossRef]
40. Thuillier, G.; Hersé, M.; Labs, D.; Foujols, T.; Peetermans, W.; Gillotay, D.; Simon, P.C.; Mandel, H. The Solar Spectral Irradiance from 200 to 2400 *nm* as Measured by the SOLSPEC Spectrometer from the Atlas and Eureca Missions. *Sol. Phys.* **2003**, *214*, 1–22. [CrossRef]
41. Wunch, D.; Wennberg, P.; Toon, G.; Connor, B.; Fisher, B.; Osterman, G.; Frankenberg, C.; Mandrake, L.; O'Dell, C.; Ahonen, P.; et al. A method for evaluating bias in global measurements of CO_2 total columns from space. *Atmos. Chem. Phys.* **2011**, *11*, 12317–12337. [CrossRef]
42. Buchwitz, M.; Reuter, M.; Schneising, O.; Hewson, W.; Detmers, R.; Boesch, H.; Hasekamp, O.; Aben, I.; Bovensmann, H.; Burrows, J.; et al. Global satellite observations of column-averaged carbon dioxide and methane: The GHG-CCI XCO_2 and XCH_4 CRDP3 data set. *Remote Sens. Environ.* **2017**, *203*, 276–295. [CrossRef]
43. Wu, L.; Hasekamp, O.; Hu, H.; Landgraf, J.; Butz, A.; de Brugh, J.a.; Aben, I.; Pollard, D.F.; Griffith, D.W.T.; Feist, D.G.; et al. Carbon dioxide retrieval from OCO-2 satellite observations using the RemoTeC algorithm and validation with TCCON measurements. *Atmos. Meas. Tech.* **2018**, *11*, 3111–3130. [CrossRef]
44. Kivi, R.; Heikkinen, P.; Kyrö, E. TCCON Data from Sodankylä (FI), Release GGG2014.R0, TCCON Data Archive, Hosted by CaltechDATA. Available online: https://doi.org/10.14291/tccon.ggg2014.sodankyla01.R0/1149280 (accessed on 28 May 2020).
45. Deutscher, N.M.; Notholt, J.; Messerschmidt, J.; Weinzierl, C.; Warneke, T.; Petri, C.; Grupe, P.; Katrynski, K. TCCON Data from Bialystok (PL), Release GGG2014.R1, TCCON Data Archive, Hosted by CaltechDATA. Available online: https://doi.org/10.14291/tccon.ggg2014.bialystok01.R1/1183984 (accessed on 28 May 2020).
46. Notholt, J.; Petri, C.; Warneke, T.; Deutscher, N.M.; Buschmann, M.; Weinzierl, C.; Macatangay, R.C.; Grupe, P. TCCON Data from Bremen (DE), Release GGG2014.R0, TCCON Data Archive, Hosted by CaltechDATA. Available online: https://doi.org/10.14291/tccon.ggg2014.bremen01.R0/1149275 (accessed on 28 May 2020).
47. Hase, F.; Blumenstock, T.; Dohe, S.; Gross, J.; Kiel, M. TCCON Data from Karlsruhe (DE), Release GGG2014.R1, TCCON Data Archive, Hosted by CaltechDATA. Available online: https://doi.org/10.14291/tccon.ggg2014.karlsruhe01.R1/1182416 (accessed on 28 May 2020).
48. Wennberg, P.O.; Roehl, C.; Wunch, D.; Toon, G.C.; Blavier, J.-F.; Washenfelder, R.; Keppel-Aleks, G.; Allen, N.; Ayers, J. TCCON Data from Park Falls (US), Release GGG2014.R0, TCCON Data Archive, Hosted by CaltechDATA. Available online: https://doi.org/10.14291/tccon.ggg2014.parkfalls01.R0/1149161 (accessed on 28 May 2020).
49. Te, Y.; Jeseck, P.; Janssen, C. TCCON Data from Paris (FR), Release GGG2014.R0, TCCON Data Archive, Hosted by CaltechDATA. Available online: https://doi.org/10.14291/tccon.ggg2014.paris01.R0/1149279 (accessed on 28 May 2020).
50. Blumenstock, T.; Hase, F.; Schneider, M.; Garcia, O.E.; Sepulveda, E. TCCON Data from Izana (ES), Release GGG2014.R0, TCCON Data Archive, Hosted by CaltechDATA. Available online: https://doi.org/10.14291/tccon.ggg2014.izana01.R0/1149295 (accessed on 28 May 2020).

51. Warneke, T.; Messerschmidt, J.; Notholt, J.; Weinzierl, C.; Deutscher, N.M.; Petri, C.; Grupe, P.; Vuillemin, C.; Truong, F.; Schmidt, M. TCCON Data from Orléans (FR), Release GGG2014.R0, TCCON Data Archive, Hosted by CaltechDATA. Available online: https://doi.org/10.14291/tccon.ggg2014.orleans01.R0/1149276 (accessed on 28 May 2020).
52. Sussmann, R.; Rettinger, M. TCCON Data from Garmisch (DE), Release GGG2014.R0, TCCON Data Archive, Hosted by CaltechDATA. Available online: https://doi.org/10.14291/tccon.ggg2014.garmisch01.R0/1149299 (accessed on 28 May 2020).
53. Morino, I.; Yokozeki, N.; Matsuzaki, T.; Horikawa, M. TCCON Data from Rikubetsu (JP), Release GGG2014.R1, TCCON Data Archive, Hosted by CaltechDATA. Available online: https://doi.org/10.14291/tccon.ggg2014.rikubetsu01.R1/1242265 (accessed on 28 May 2020).
54. Wennberg, P.O.; Wunch, D.; Roehl, C.; Blavier, J.-F.; Toon, G.C.; Allen, N. TCCON Data from Lamont (US), Release GGG2014.R1, TCCON Data Archive, Hosted by CaltechDATA. Available online: https://doi.org/10.14291/tccon.ggg2014.lamont01.R1/1255070 (accessed on 28 May 2020).
55. Morino, I.; Matsuzaki, T.; Horikawa, M. TCCON Data from Tsukuba (JP), 125HR, Release GGG2014.R1, TCCON Data Archive, Hosted by CaltechDATA. Available online: https://doi.org/10.14291/tccon.ggg2014.tsukuba02.R1/1241486 (accessed on 28 May 2020).
56. Kawakami, S.; Ohyama, H.; Arai, K.; Okumura, H.; Taura, C.; Fukamachi, T.; Sakashita, M. TCCON Data from Saga (JP), Release GGG2014.R0, TCCON Data Archive, Hosted by CaltechDATA. Available online: https://doi.org/10.14291/tccon.ggg2014.saga01.R0/1149283 (accessed on 28 May 2020).
57. Griffith, D.W.T.; Deutscher, N.M.; Velazco, V.A.; Wennberg, P.O.; Yavin, Y.; Keppel-Aleks, G.; Washenfelder, R.; Toon, G.C.; Blavier, J.-F.; Paton-Walsh, C.; et al. TCCON Data from Darwin (AU), Release GGG2014.R0, TCCON Data Archive, Hosted by CaltechDATA. Available online: https://doi.org/10.14291/tccon.ggg2014.darwin01.R0/1149290 (accessed on 28 May 2020).
58. Griffith, D.W.T.; Velazco, V.A.; Deutscher, N.M.; Paton-Walsh, C.; Jones, N.B.; Wilson, S.R.; Macatangay, R.C.; Kettlewell, G.C.; Buchholz, R.R.; Riggenbach, M. TCCON Data from Wollongong (AU), Release GGG2014.R0, TCCON Data Archive, Hosted by CaltechDATA. Available online: https://doi.org/10.14291/tccon.ggg2014.wollongong01.R0/1149291 (accessed on 28 May 2020).
59. Morino, I.; Velazco, V.A.; Hori, A.; Uchino, O.; Griffith, D.W.T. TCCON Data from Burgos, Ilocos Norte (PH), Release GGG2014.R0, TCCON Data Archive, Hosted by CaltechDATA. Available online: https://doi.org/10.14291/tccon.ggg2014.burgos01.R0 (accessed on 28 May 2020).
60. Iraci, L.T.; Podolske, J.R.; Hillyard, P.W.; Roehl, C.; Wennberg, P.O.; Blavier, J.-F.; Landeros, J.; Allen, N.; Wunch, D.; Zavaleta, J.; et al. TCCON data from Edwards (US), Release GGG2014.R1, TCCON Data Archive, Hosted by CaltechDATA. Available online: https://doi.org/10.14291/tccon.ggg2014.edwards01.R1/1255068 (accessed on 28 May 2020).
61. Wennberg, P.O.; Roehl, C.M.; Blavier, J.-F.; Wunch, D.; Allen, N.T. TCCON Data from Jet Propulsion Laboratory (US), 2011, Release GGG2014.R1, TCCON Data Archive, Hosted by CaltechDATA. Available online: https://doi.org/10.14291/tccon.ggg2014.jpl02.R1/1330096 (accessed on 28 May 2020).
62. Wennberg, P.O.; Wunch, D.; Roehl, C.M.; Blavier, J.-F.; Toon, G.C.; Allen, N.T. TCCON Data from Caltech (US), Release GGG2014.R1, TCCON Data Archive, Hosted by CaltechDATA. Available online: https://doi.org/10.14291/tccon.ggg2014.pasadena01.R1/1182415 (accessed on 28 May 2020).
63. Sussmann, R.; Rettinger, M. TCCON Data from Zugspitze (DE), Release GGG2014.R1, TCCON Data Archive, Hosted by CaltechDATA. Available online: https://doi.org/10.14291/tccon.ggg2014.zugspitze01.R1 (accessed on 28 May 2020).
64. Crisp, D.; Pollock, H.R.; Rosenberg, R.; Chapsky, L.; Lee, R.A.M.; Oyafuso, F.A.; Frankenberg, C.; O'De, C.W.; Bruegge, C.J.; Doran, G.B.; et al. The on-orbit performance of the Orbiting Carbon Observatory-2 (OCO-2) instrument and its radiometrically calibrated products. *Atmos. Meas. Tech.* **2017**, *10*, 59–81. [CrossRef]